Odd-even layer-number effect of valence-band spin splitting in WTe_2

Masato Sakano,[1,*] Yuma Tanaka,[1,*] Satoru Masubuchi,[2,*] Shota Okazaki,[3] Takuya Nomoto,[1] Atsushi Oshima,[1] Kenji Watanabe,[4] Takashi Taniguchi,[5] Ryotaro Arita,[1,6] Takao Sasagawa,[3] Tomoki Machida,[2] and Kyoko Ishizaka[1,6]

[1]*Quantum-Phase Electronics Center and Department of Applied Physics, The University of Tokyo, Bunkyo-ku, Tokyo, 113–8656, Japan*

[2]*Institute of Industrial Science, The University of Tokyo, Meguro-ku, Tokyo 153–8505, Japan*

[3]*Materials and Structures Laboratory, Tokyo Institute of Technology, Yokohama, Kanagawa, 226–8503, Japan*

[4]*Research Center for Functional Materials, National Institute for Materials Science, 1-1 Namiki, Tsukuba 305-0044, Japan*

[5]*International Center for Materials Nanoarchitectonics, National Institute for Materials Science, 1-1 Namiki, Tsukuba 305-0044, Japan*

[6]*RIKEN Center for Emergent Matter Science (CEMS), Wako, Saitama, 351-0198, Japan*

(Received 18 October 2021; revised 13 May 2022; accepted 19 May 2022; published 27 June 2022)

When a crystal becomes thin to the atomic level, peculiar phenomena discretely depending on its layer numbers (n) start to appear. Here, we investigate the electronic band dispersions of multilayer WTe_2 (2–5 layers), by performing laser-based microfocused angle-resolved photoelectron spectroscopy on exfoliated flakes sorted by n. We observe that the holelike valence bands start to cross the Fermi level when the number of layers is increased from 2- to 3 layers, which should be related to the insulator-semimetal transition, as well as the 30–70-meV spin splitting of valence bands manifesting in even n as a signature of stronger structural asymmetry. Our result fully demonstrates the possibility of the large energy-scale band and spin manipulation through the finite-n stacking procedure.

DOI: 10.1103/PhysRevResearch.4.023247

Two-dimensional (2D) materials science based on transition-metal dichalcogenides (TMD) has been actively pursued following the discovery of graphene [1]. One of the fundamental and fascinating phenomena is the spin-valley polarized state that gives rise to a variety of Berry-curvature related properties in monolayers of 2H-type group-VI TMD semiconductors such as WSe_2 [2–7]. This occurs as a consequence of the C_3 inversion-symmetry breaking which couples the spin and the valence-band valley degrees of freedom at the K point via the spin-orbit interaction. Since the layer stacking of 2H-TMD is antiphase with 180° rotation, the spin-valley polarization cancels out in bulk, but appears as the curious even-odd layer-number (n) effect when it becomes atomically thin [7–9]. In general, similar effects are expected in systems with antiphase stacking. Here, we focus on T_d-WTe_2 [10,11] as another example. Figure 1 shows the characteristics of T_d-WTe_2 compared to 2H-WSe_2. T_d-WTe_2 monolayer is characterized by the network of edge-sharing WTe_6 octahedra, which is often classified as 1T- or CdI_2-type in the TMD family [Fig. 1(a)]. However, bulk WTe_2 differs from the usual 1T-TMD in that it has the antiphase layer stacking associated with the strong anisotropic distortion of the octahedral network. To show the framework of this peculiar stacking, Fig. 1(b) presents a significantly simplified schematic of WTe_2 along the yz (mirror) plane, by ignoring any intralayer distortion beyond D_{3d} symmetry. The orange triangles represent the orientation of Te triangular networks. In this model, the monolayer has inversion symmetry, but this is lost in the bilayer due to the antiphase stacking [12]. This is the opposite behavior to that of 2H-WSe_2 as shown in Figs. 1(c) and 1(d), and different type of even-odd layer-number dependence can be expected in WTe_2.

WTe_2 is also known as a material whose physical property exhibits a distinctive variance from bulk towards monolayer. Bulk WTe_2 actually has a complicated structure (space group $Pnm2_1$) with z-axis polarity, unlike the above-mentioned simplified picture. It is a charge-compensated polar semimetal [13] and had been predicted as a type-II Weyl semimetal [14–16]. In contrast, mono- and 2-layer WTe_2 are reported as insulators with small band gaps [17–19]. Particularly, the monolayer WTe_2 is known as the 2D quantum spin Hall insulator [20,21]. Regarding the crystal structure, although the monolayer WTe_2 is centrosymmetric, z-axis polarization appears in $n \geqslant 2$ multilayer WTe_2 which is associated with the alternative y shifts of C_2 axes on stacking [see the "realistic" case in Fig. 1(b)] [18,19,22–27]. Thus, the point group of multilayer WTe_2 becomes C_s irrespective of n [12]. This inversion-symmetry breaking leads to unique phenomena such as the nonlinear anomalous Hall effect [22,24–27] and the ferroelectric switching related to Berry-curvature dipole [18,27]. Furthermore, the even-odd layer-number dependence in the ferroelectric switching was theoretically predicted [12], and recently experimentally demonstrated in the 3- and 4-layer WTe_2 [27]. These studies on WTe_2 have been mostly done by comparing the transport properties on microdevices with the band calculations. We should note that band

*These authors contributed equally to this work.

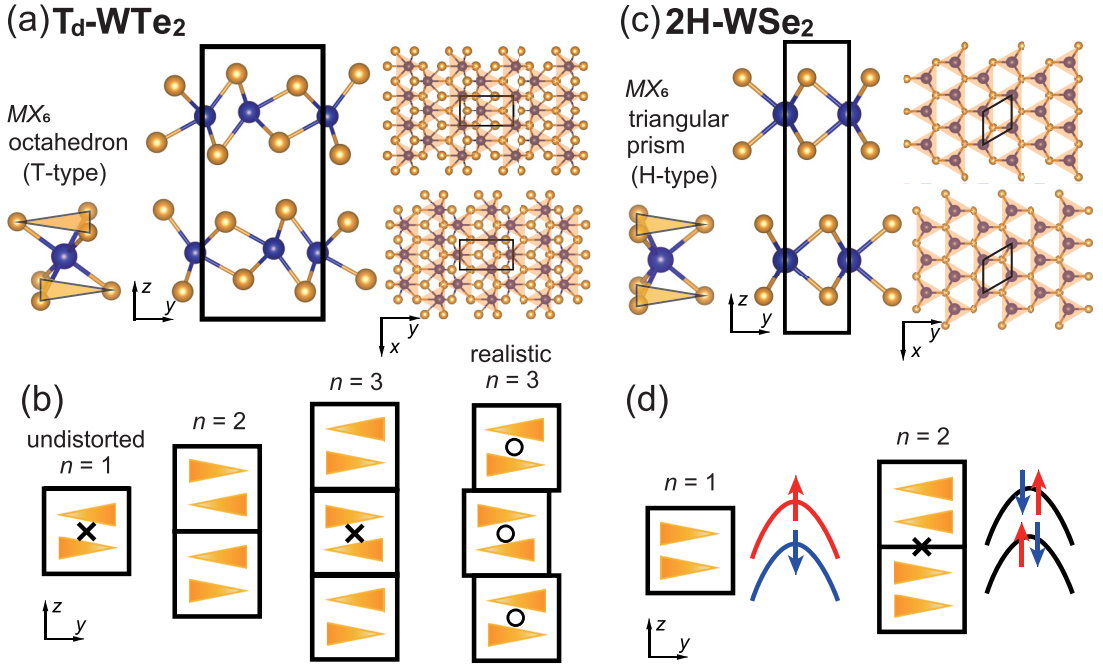

FIG. 1. (a) The octahedral coordination for the T-type transition-metal dichalcogenides, side view of the bulk crystal structure of $2H$-WTe_2, and top views of the adjacent WTe_2 layers. The transparent orange triangles indicate the orientation of Te triangular networks. (b) Left three panels: Side views of the simplified schematic models for 1–3-layer WTe_2 where the structural asymmetry within the monolayer is ignored [14]. The black block and orange triangles represent each unit of the WTe_2 layer and the orientations of Te triangular networks within a layer. The cross markers (×) represent the C_2 axes. Right panel: A schematic model for the realistic crystal structure of 3-layer WTe_2. The open-circle markers (○) indicate the "C_2 axes" within each WTe_2 layer, which shift slightly along y directions. (c) The prismatic coordination for the H-type TMDs and the side and top views of $2H$-WSe_2 are shown in the same manner as in (a). (d) Schematics of the spin-valley coupled electronic structure for monolayer WSe_2 and the spin-degenerate electronic structure for 2-layer WSe_2 because of the recovery of inversion symmetry.

calculations are making great progress, and a variety of methods are used for atomically thin flakes. Still, there are many difficulties specific to flakes: the lack of structural information, the computational cost of handling the finite-size slabs, and so on. Thus, the experimental clarification of the band structures is highly desired for thoroughly understanding the n-dependent properties and the effect of stacking.

In this work, we prepared the series of graphene-encapsulated WTe_2 flakes ideally sorted by layer numbers and clarified the electronic band structures in 2–5-layer WTe_2 by using the laser-based microfocused angle-resolved photoemission spectroscopy (μ-ARPES) system. It clearly revealed the insulator-semimetal transition realized between the 2- and 3-layers which agrees well with the transport properties [6], and the striking even-odd effect in the n dependence of the spin-band splitting.

Figure 2(a) shows an optical microscope image of a typical sample. The encapsulation by the graphene protects the surface from degradation while transporting [19,28]. Layer-number n of WTe_2 flakes were first distinguished by image analysis [29–31], which were further confirmed by the obtained ARPES spectra. The upper panels in Fig. 2(c) show the 2–5-layer WTe_2 flakes (depicted by white frames) used to obtain the corresponding ARPES images in the lower panels, respectively. As n increases, the number of the bands clearly increases. Figure 2(d) shows the energy distribution curves (EDCs) at $k_x = 0$ for 2–5-layer WTe_2. From the number of the bands in the energy range of -0.15 to -0.45 eV, we can determine n as it corresponds well with the quantized eigenstates. From this we can confirm that the 2–5-layer WTe_2 flake samples are successfully prepared and separately measured by μ-ARPES [32].

First, we focus on the electronic structures near the Fermi level (E_F). Figures 3(a)–3(d) show the ARPES images for 2–5-layer WTe_2. Here, the k_x axis corresponds to the Γ-X direction, where the semimetallic characters with hole- and electron bands are most well observed in bulk WTe_2 [13–16,33,34]. Band hybridization and/or folded replica bands that may arise from graphene encapsulation have not been observed in their momentum regions. In these figures, we can clearly distinguish the n-dependent evolution of the holelike band dispersions around $k_x \simeq -0.2$ Å^{-1}, seemingly varying from being fully occupied ($n = 2$), nearly touching E_F ($n = 3$), to apparently crossing E_F ($n = 4$ and 5).

In 2-layer WTe_2, the valence-band maximum is located at Γ, and energy position is estimated to be $-28(10)$ meV, where the intensity is weak. We note that the holelike flat-band feature around $k_x \simeq -0.2$ Å^{-1} and -35 meV is in a good agreement with the previous ARPES result [19]. For comparison, we show in Fig. 2(e) the result of band calculation utilizing the Heyd-Scuseria-Ernzerhof (HSE) [35] hybrid functional (red curves) overlaid with that of the Perdew-Burke-Ernzerhof generalized gradient approximation (GGA-PBE) [36] (dashed blue curves). Although the holelike bands around -0.2 Å^{-1} are more dispersive than those experimentally obtained, the observed small band gap (60–110 meV) between the electron-like (above E_F) and the holelike band (below E_F) is suitably reproduced by the HSE calcula-

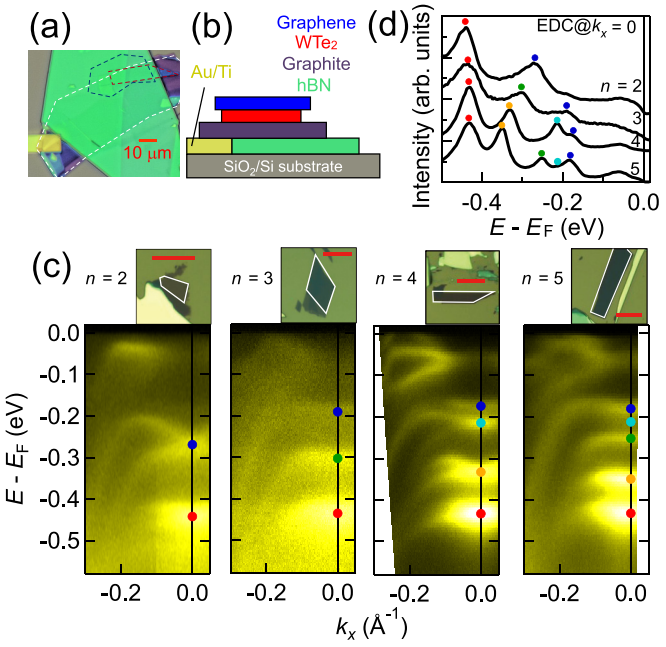

FIG. 2. (a) Optical microscope image of the fabricated graphene/WTe_2/graphite/h-BN heterostructure sample. (b) Schematic of the fabricated sample. (c) Upper panels: The optical microscope images of the 2–5-layer WTe_2 flakes (white frames) used for ARPES. The red bars represent the 10-mm length. Lower panels: Obtained ARPES images for 2–5-layer WTe_2. The makers (•) indicate the positions of the intensity peaks at $k_x = 0$ [see (d)]. (d) EDCs at $k_x = 0$ presented for 2–5 layers.

tion (∼40 meV), in contrast to GGA-PBE. HSE calculation shows good agreement with the ARPES result, indicating that the effect of graphene encapsulation (e.g., band hybridization, strain effect, etc.) is not seriously strong in the present case. Thus, our result indicates that 2-layer WTe_2 belongs to the gapped insulator phase. To experimentally detect the possible electron-like band above E_F, we further performed ARPES at room temperature [Fig. 3(f)]. Dividing by the 300 K Fermi-Dirac distribution function allows us to visualize the electronic structures above E_F. Figure 3(g) shows the EDCs extracted from the ARPES image in Fig. 3(f), with respective peak positions plotted by markers. In the $k_x = 0 - 0.2$ Å^{-1} region, the dispersion of the valence-band edge appears around 30–60 meV below E_F, whereas the contribution of the electron band bottom shows up around $k_x = -0.2$ to -0.27 Å^{-1} region at ∼50 meV above E_F.

To similarly discuss 3-layer WTe_2, we show in Figs. 3(h) and 3(i) the band calculation (HSE and GGA-PBE) and the ARPES image combining the data taken with the $p-$ ($k_x < -0.25$ Å^{-1}) and s-polarized ($k_x > -0.25$ Å^{-1}) lights, respectively. The electron band appears stronger with p-polarization setup because of the matrix-element effect. Figure 3(j) shows the EDCs extracted from the ARPES image in Fig. 3(i), with the markers indicating the peak positions. At $k_x = -0.32$ and -0.36 Å^{-1}, faint but finite ARPES intensities [○ in Fig. 3(j)] show up near E_F, as compared to the $k_x > -0.28$ Å^{-1} region [32,37]. It corresponds to the bottom of the conduction band crossing E_F [○ in Fig. 3(i)]. The HSE calculation for 3-layer WTe_2 [red curve in Fig. 3(h)] also well reproduces such overlaps of the electron- and hole bands at E_F. Our ARPES results thus confirm that HSE better reproduces the near-E_F electronic structure at least for $n = 2, 3$. It also shows that the insulator-semimetal transition is realized between 2- and 3 layer, being consistent with the transport property [17].

Now we present the n-dependent spin splitting of valence bands. Figures 4(a)–4(d) show curvature plots [37] for the ARPES images of the 2–5-layer WTe_2 along k_x corresponding to Fig. 2(c) for better visualization. Here, we focus on the energy range of -0.15 to -0.5 eV. On the right side ($k_x \geqslant 0$), the peak positions of ARPES intensities estimated from the EDCs and the momentum distribution curves (MDCs) are plotted with markers • and ♦, respectively. When the spin splitting is small, it is hard to determine whether the spectral peak consists of single or double components. In such a case we place a marker at the peak position estimated by assuming a single component, together with a bar whose ends represent the peak positions estimated by assuming double components. The obtained band dispersions are then indexed from the lower-energy side as #i ($i = 1-n$). As we can see in Figs. 3(a)–3(d), the bands in 2- and 4-layer WTe_2 clearly exhibit the notable band splitting. This can be regarded as the strong evidence for inversion-symmetry breaking which lifts the spin degeneracy through the spin-orbit interaction. In contrast, 3- and 5-layer WTe_2 exhibit small or indetectable band splitting as shown in Figs. 4(b) and 4(d). Such clear even-odd effect in the n dependence is what we naively expected in Fig. 1(b). Nevertheless, we should note again that the real multilayer WTe_2 has more complicated structures with the noncentrosymmetric point-group symmetry C_s commonly for $n \geqslant 2$. Thus, we need careful and quantitative discussion beyond the symmetry arguments.

Here we compare the experimental result with the GGA-PBE slab calculation that can fully handle 2–5-layer WTe_2. Figures 4(e)–4(h) show the calculated band dispersions, with the red-blue colored weights indicating the spin polarizations along y (S_y, left side) and z (S_z, right side). As increasing n, the number of valence bands also correspondingly increases. When we focus on the S_y and S_z components as well as the band splitting, there are certain quantitative differences between the even- and odd-n cases. One is that the spin splitting obtained in even n is apparently larger than those in odd n. Another difference is found in the spin component of the band dispersions showing the splitting. For example, when we look at bands #1,2 for 2-5-layer WTe_2, the main spin component is predominantly S_z for 2- and 4 layer, while it rather appears in S_y for 3- and 5 layer. Similar trends are also confirmed for many other bands #i. In general, the spin-orbit interaction works as an effective magnetic field that is perpendicular to the potential gradient and to the momentum of electrons [7,38]. It thus indicates that on the k_x axis, S_y- and S_z components are, respectively, induced by the local potential gradient along z and y in the crystal structure. In the even-n cases, the S_z polarization should be arising from the in-plane potential of the Te triangular network, whereas in odd-n cases this effect is weakened. The result of GGA-PBE calculations thus suggests that the characteristics of the potential gradient associated with the spatial asymmetry alternately changes as n is increased, resulting in the even-odd effect in the n. The HSE

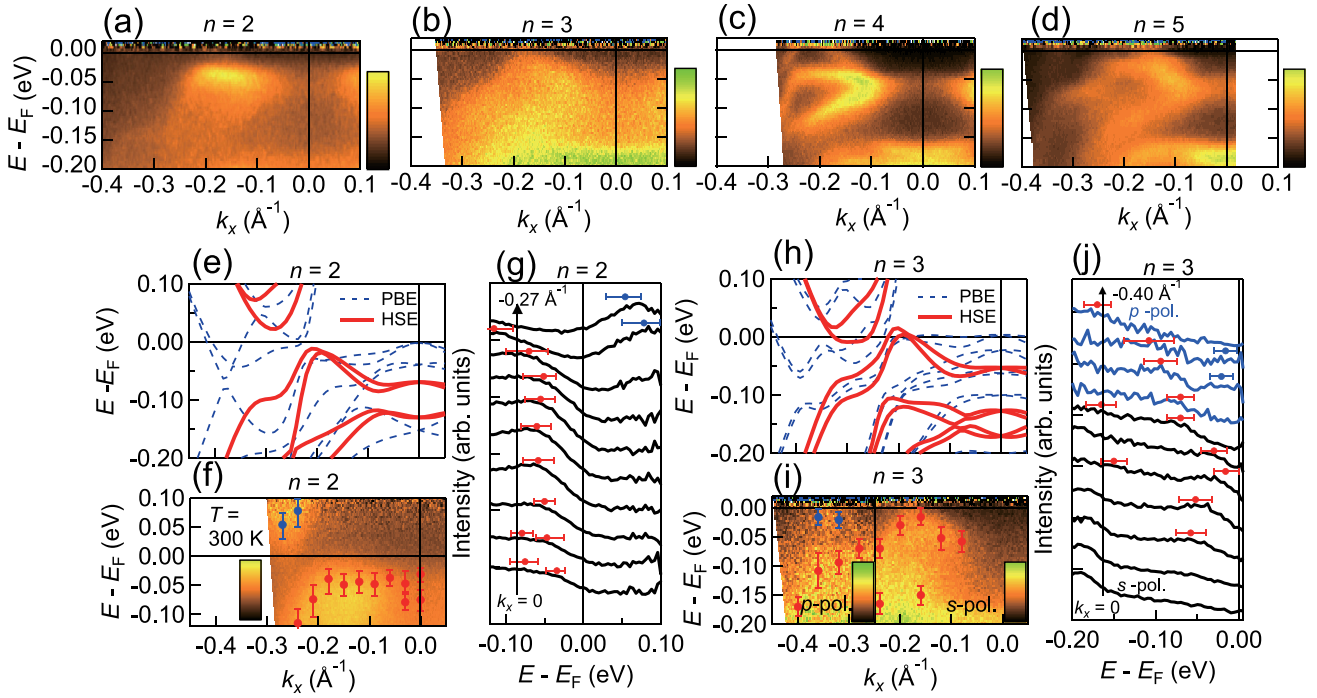

FIG. 3. (a)–(d) ARPES images near the E_F for 2–5-layer WTe_2. (e) Band calculations on 2-layer WTe_2 obtained by using the GGA-PBE (blue dashed curves) and HSE hybrid functional (red solid curves). (f) ARPES image for 2-layer WTe_2 taken at room temperature. (g) EDCs extracted from the ARPES image for 2-layer WTe_2 in (f). The red (blue) markers represent the positions of the intensity peaks for the valence (conduction) bands, and the error bars represent the uncertainty of the peak position. (h) Band calculations for 3-layer WTe_2 in the same manner as in (e). (i) ARPES image for 3-layer WTe_2 presented by combining the data using *p*- and *s*-polarized lights. (j) EDCs extracted from the ARPES image for 3-layer WTe_2 in (i). The red-filled (blue-empty) circle markers indicate the positions of the intensity peaks for valence (conduction) bands, and the error bars represent the uncertainty of the peak position.

calculation on 2- and 3-layer WTe_2 also shows the similar trend [32]. We note that the calculations performed here use the WTe_2 slab models with the atomic coordinates fixed to those in the bulk crystal [11]. It thus rules out any influences related to atomic relaxations or reconstructions. Our result suggests that the peculiar antiphase stacking of WTe_2 [see Fig. 1(a)] should be playing the dominant role on the even-odd effect of the spin splitting, through the structural asymmetry as reflected in S_y and S_z.

Finally, to demonstrate the *n*-dependent spin-band splitting more quantitatively, we focus on the EDCs at $k_x = -0.1$ Å^{-1} as shown in Fig. 4(i). The markers, horizontal bars, and the band indices #*i* are given in the similar manner as those in Figs. 4(a)–4(d). The two-peak structures for bands #*i* can be separately observed for even-*n* samples, whereas they are hard to discern in odd-*n* cases. In Fig. 4(j), the energies of the band splitting estimated from the separation of these peak positions in Fig. 4(i) are summarized (solid circles •) with those similarly obtained by GGA-PBE calculations at $k_x = -0.1$ Å^{-1} (open circles ○). The values of band splitting in 2- and 4-layer WTe_2 are mostly spreading in the range of 20–70 meV, whereas those in 3- and 5 layer are limited within the range of 0–30 meV except for the calculated band #1 in $n = 5$. This result clearly shows the peculiar even-odd effect in *n*-dependent band splitting, and the larger spin splitting with the out-of-plane spin S_z component in even *n*.

To summarize, we investigated the *n*-dependent band structures in few-layer WTe_2. We observed that the holelike bands cross the Fermi level between 2- and 3 layer, suggesting the insulator-semimetal transition consistent with the previous transport measurements. Furthermore, we found the strong even-odd *n* dependence of the spin splitting in ∼70-meV scale, originating from the in-plane potential gradient of Te triangular network. It successfully demonstrates the finite-*n* effect appearing in the antiphase stacking system and raises the possibility of the large energy-scale band and spin manipulation through the finite-*n* stacking procedure.

ACKNOWLEDGMENTS

We thank Y. Yanase for fruitful discussion. This research was partly supported by a CREST project (Grants No. JPMJCR15F3, No. JPMJCR16F2, and No. JPMJCR20B4) from the Japan Science and Technology Agency (JST) and Japan Society for the Promotion of Science KAKENHI (Grants-in-Aid for Scientific Research) (Grants No. JP20H00127, No. JP20H00354, No. JP20H01834, No. JP21H05232, No. JP21H05233, No. JP21H05234, No. JP21H05235, and No. JP21H05236).

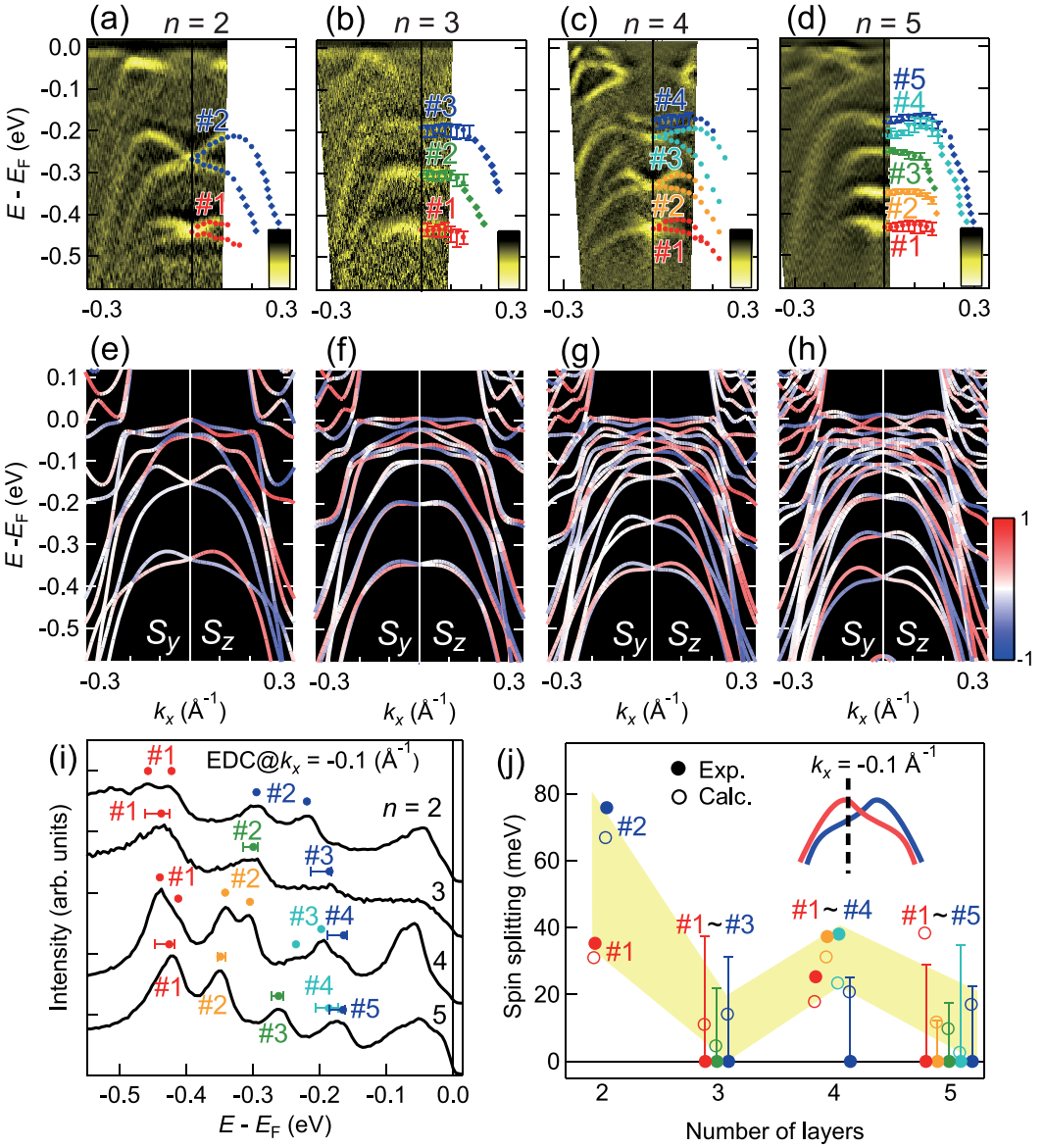

FIG. 4. (a)–(d) Images obtained by the curvature analysis [37] for the ARPES images of 2–5-layer WTe_2 shown in Fig. 2(c). Symbols • and ♦ represent the peak positions obtained by fitting the EDCs and the momentum distribution curves (MDCs), respectively. (e)–(h) Band calculations along the k_x direction by using GGA-PBE. The slab structures consist of using the atomic coordinates of the bulk crystal [11] without any relaxations. The band dispersions in $k_x < 0$ and $k_x > 0$ are indicated by the color of the spin y- and z components (S_y and S_z), respectively, according to the color scale on the right of panel (h). The spin axes are defined by the orthogonal axes (xyz) shown in Fig. 1(a). (i) EDCs at $k_x = -0.1$ Å^{-1} for 2–5-layer WTe_2. (j) n dependence of the energy of the band splitting obtained by the ARPES (•) and the calculation (○). The inset represents that the energy of the spin splitting is estimated at $k_x = -0.1$ Å^{-1}. Markers (•) represent the peak positions estimated by assuming a single component, together with a bar whose ends represent the peak positions estimated by assuming double components.

[1] K. S. Novoselov, A. K. Geim, S. V. Morozov, D. Jiang, Y. Zhang, S. V. Dubonos, I. V. Grigorieva, and A. A. Firsov, Electric field effect in atomically thin carbon films, Science **306**, 666 (2004).

[2] D. Xiao, G. Liu, W. Feng, X. Xu, and W. Yao, Coupled Spin and Valley Physics in Monolayers of MoS_2 and Other Group-VI Dichalcogenides, Phys. Rev. Lett. **108**, 196802 (2012).

[3] H. Zeng, J. Dai, W. Yao, D. Xiao, and X. Cui, Valley polarization in MoS_2 monolayers by optical pumping, Nat. Nanotechnol. **7**, 490 (2012).

[4] K. F. Mak, K. He, J. Shan, and T. F. Heinz, Control of valley polarization in monolayer MoS_2 by optical helicity, Nat. Nanotechnol. **7**, 494 (2012).

[5] T. Cao, G. Wang, W. Han, H. Ye, C. Zhu, J. Shi, Q. Niu, P. Tan, E. Wang, B. Liu, and J. Feng, Valley-selective circular dichroism of monolayer molybdenum disulphide, Nat. Commun. **3**, 887 (2012).

[6] A. M. Jones, H. Yu, N. J. Ghimire, S. Wu, G. Aivazian, J. S. Ross, B. Zhao, J. Yan, D. G. Mandrus, D. Xiao, W. Yao, and X. Xu, Optical generation of excitonic valley coherence in monolayer WSe_2, Nat. Nanotechnol. **8**, 634 (2013).

[7] R. Suzuki, M. Sakano, Y. J. Zhang, Akashi R, D. Morikawa, A. Harasawa, K. Yaji, K. Kuroda, K. Miyamoto, T. Okuda, K. Ishizaka, R. Arita, and Y. Iwasa, Valley-dependent spin polarization in bulk MoS_2 with broken inversion symmetry, Nat. Nanotechnol. **9**, 611 (2014).

[8] Y. Li, Y. Rao, K. F. Mak, Y. You, S. Wang, C. R. Dean, and T. F. Heinz, Probing symmetry properties of few-layer MoS_2 and h-BN by optical second-harmonic generation, Nano Lett. **13**, 3329 (2013).

[9] Z. Wu, S. Xu, H. Lu, A. Khamoshi, G.-B. Liu, T. Han, Y. Wu, J. Lin, G. Long, Y. He, Y. Cai, Y. Yao, F. Zhang, and N. Wang, Even–odd layer-dependent magnetotransport of high-mobility Q-valley electrons in transition metal disulfides, Nat. Commun. **7**, 12955 (2016).

[10] B. E. Brown, The crystal structures of WTe_2 and high-temperature $MoTe_2$, Acta Crystallogr. **20**, 268 (1966).

[11] A. Mar, S. Jobic, and J. Ibers, Metal-metal vs tellurium-tellurium bonding in WTe_2 and its ternary variants $TaIrTe_4$ and $NbIrTe_4$, J. Am. Chem. Soc. **114**, 8963 (1992).

[12] H. Wang and X. Qian, Ferroelectric nonlinear anomalous Hall effect in few-layer WTe_2, npj Comput. Mater. **5**, 119 (2019).

[13] M. N. Ali, J. Xiong, S. Flynn, J. Tao, Q. D. Gibson, L. M. Schoop, T. Liang, N. Haldolaarachchige, M. Hirschberger, N. P. Ong, and R. J. Cava, Large, non-saturating magnetoresistance in WTe_2, Nature (London) **514**, 205 (2014).

[14] A. A. Soluyanov, D. Gresch, Z. Wang, Q. Wu, M. Troyer, X. Dai, and B. A. Bernevig, Type-II Weyl semimetals, Nature (London) **527**, 495 (2015).

[15] N. P. Armitage, E. J. Mele, and A. Vishwanath, Weyl and Dirac semimetals in three-dimensional solids, Rev. Mod. Phys. **90**, 015001 (2018).

[16] P. K. Das, D. D. Sante, F. Cilento, C. Bigi, D. Kopic, D. Soranzio, A. Sterzi, J. A. Krieger, I. Vobornik, J. Fujii, T. Okuda, V. N. Strocov, M. B. H. Breese, F. Parmigiani, G. Rossi, S. Picozzi, R. Thomale, G. Sangiovanni, R. J. Cava, and G. Panaccione, Electronic properties of candidate type-II Weyl semimetal WTe_2. A review perspective, Electron. Struct. **1**, 014003 (2019).

[17] Z. Fei, T. Palomaki, S. Wu, W. Zhao, X. Cai, B. Sun, P. Nguyen, J. Finney, X. Xu, and D. H. Cobden, Edge conduction in monolayer WTe_2, Nat. Phys. **13**, 677 (2017).

[18] Z. Fei, W. Zhao, T. A. Palomaki, B. Sun, M. K. Miller, Z. Zhao, J. Yan, X. Xu, and D. H. Cobden, Ferroelectric switching of a two-dimensional metal, Nature (London) **560**, 336 (2018).

[19] I. Cucchi, I. Gutiérrez-Lezama, E. Cappelli, S. M. Walker, F. Y. Bruno, G. Tenasini, L. Wang, N. Ubrig, C. Barreteau, E. Giannini, M. Gibertini, A. Tamai, A. F. Morpurgo, and F. Baumberger, Microfocus laser–angle-resolved photoemission on encapsulated mono-, bi-, and few-layer 1T'-WTe_2, Nano Lett. **19**, 554 (2019).

[20] S. Tang, C. Zhang, D. Wong, Z. Pedramrazi, H.-Z. Tsai, C. Jia, B. Moritz, M. Claassen, H. Ryu, S. Kahn, J. Jiang, H. Yan, M. Hashimoto, D. Lu, R. G. Moore, C.-C. Hwang, C. Hwang, Z. Hussain, Y. Chen, M. M. Ugeda, Z. Liu, X. Xie, T. P. Devereaux, M. F. Crommie, S.-K. Mo, and Z.-X. Shen, Quantum spin Hall state in monolayer 1T'-WTe_2, Nat. Phys. **13**, 683 (2017).

[21] S. Wu, V. Fatemi, Q. D. Gibson, K. Watanabe, T. Taniguchi, R. J. Cava, and P. Jarillo-Herrero, Observation of the quantum spin Hall effect up to 100 kelvin in a monolayer, Science **359**, 76 (2018).

[22] I. Sodemann and L. Fu, Quantum Nonlinear Hall Effect Induced by Berry Curvature Dipole in Time-Reversal Invariant Materials, Phys. Rev. Lett. **115**, 216806 (2015).

[23] S.-Y. Xu, Q. Ma, H. Shen, V. Fatemi, S. Wu, T. R. Chang, G. Chang, A. M. Mier Valdivia, C.-K. Chan, Q. D. Gibson, J. Zhou, Z. Liu, K. Watanabe, T. Taniguchi, H. Lin, R. J. Cava, L. Fu, N. Gedik, and P. Jarillo-Herrero, Electrically switchable Berry curvature dipole in the monolayer topological insulator WTe_2, Nat. Phys. **14**, 900 (2018).

[24] Q. Ma, S.-Y. Xu, H. Shen, D. MacNeill, V. Fatemi, T. R. Chang, A. M. Mier Valdivia, S. Wu, Z. Du, C. H. Hsu, S. Fang, Q. D. Gibson, K. Watanabe, T. Taniguchi, R. J. Cava, E. Kaxiras, H. Z. Lu, H. Lin, L. Fu, N. Gedik, and P. Jarillo-Herrero, Observation of the nonlinear Hall effect under time-reversal-symmetric conditions, Nature (London) **565**, 337 (2019).

[25] L.-K. Shi and J. C. W. Song, Symmetry, spin-texture, and tunable quantum geometry in a WTe_2 monolayer, Phys. Rev. B **99**, 035403 (2019).

[26] K. Kang, T. Li, E. Sohn, J. Shan, and K. F. Mak, Nonlinear anomalous Hall effect in few-layer WTe_2, Nat. Mater. **18**, 324 (2019).

[27] J. Xiao, Y. Wang, H. Wang, C. D. Pemmaraju, S. Wang, P. Muscher, E. J. Sie, C. M. Nyby, T. P. Devereaux, X. Qian, X. Zhang, and A. M. Lindenberg, Berry curvature memory through electrically driven stacking transitions, Nat. Phys. **16**, 1028 (2020).

[28] N. R. Wilson, P. V. Nguyen, K. Seyler, P. Rivera, A. J. Marsden, Z. P. Laker, G. C. Constantinescu, V. Kandyba, A. Barinov, N. D. Hine, X. Xu, and D. H. Cobden, Determination of band offsets, hybridization, and exciton binding in 2D semiconductor heterostructures, Sci. Adv. **3**, e1601832 (2017).

[29] S. Masubuchi, M. Morimoto, S. Morikawa, M. Onodera, Y. Asakawa, K. Watanabe, T. Taniguchi, and T. Machida, Autonomous robotic searching and assembly of two-dimensional crystals to build van der Waals superlattices, Nat. Commun. **9**, 1413 (2018).

[30] S. Masubuchi, E. Watanabe, Y. Seo, S. Okazaki, T. Sasagawa, K. Watanabe, T. Taniguchi, and T. Machida, Deep-learning-based image segmentation integrated with optical microscopy for automatically searching for two-dimensional materials, npj 2D Mater. Appl. **4**, 3 (2020).

[31] S. Masubuchi and T. Machida, Classifying optical microscope images of exfoliated graphene flakes by data-driven machine learning, npj 2D Mater. Appl. **3**, 4 (2019).

[32] See Supplemental Material at http://link.aps.org/supplemental/10.1103/PhysRevResearch.4.023247 for details of the μ-ARPES measurement, sample fabrication procedure, calculations, and curvature analyses.

[33] I. Pletikosic, M. N. Ali, A. V. Fedorov, R. J. Cava, and T. Valla, Electronic Structure Basis for the Extraordinary Magnetoresistance in WTe_2, Phys. Rev. Lett. **113**, 216601 (2014).

[34] Z. Zhu, X. Lin, J. Liu, B. Fauqué, Q. Tao, C. Yang, Y. Shi, and K. Behnia, Quantum Oscillations, Thermoelectric Coefficients, and the Fermi Surface of Semimetallic WTe_2, Phys. Rev. Lett. **114**, 176601 (2015).

[35] J. Heyd, G. E. Scuseria, and M. Ernzerhof, Hybrid functionals based on a screened Coulomb potential, J. Chem. Phys. **118**, 8207 (2003).

[36] J. P. Perdew, K. Burke, and M. Ernzerhof, Generalized Gradient Approximation Made Simple, Phys. Rev. Lett. **77**, 3865 (1996).

[37] P. Zhang, P. Richard, T. Qian, Y.-M. Xu, X. Dai, and H. Ding, A precise method for visualizing dispersive features in image plots, Rev. Sci. Instrum. **82**, 043712 (2011).

[38] K. Ishizaka, M. S. Bahramy, H. Murakawa, M. Sakano, T. Shimojima, T. Sonobe, K. Koizumi, S. Shin, H. Miyahara, A. Kimura, K. Miyamoto, T. Okuda, H. Namatame, M. Taniguchi, R. Arita, N. Nagaosa, K. Kobayashi, Y. Murakami, R. Kumai, Y. Kaneko, Y. Onose, and Y. Tokura, Giant Rashba-type spin splitting in bulk BiTeI, Nat. Mater. **10**, 521 (2011).